



ORIGINAL RESEARCH ARTICLE

Comparative Study on the Microstructure, Wear Behavior, and Corrosion Performance of Iron-Based and Cobalt-Based Coatings Fabricated by Laser Cladding

F. Jin, S. Zhang, C.L. Wu, C.H. Zhang, X.Y. Sun, and X.L. Bai

Submitted: 14 March 2023 / Revised: 9 August 2023 / Accepted: 23 September 2023

In this paper, two kinds of coatings (iron-based and cobalt-based) were successfully prepared on the surface of AISI 304 stainless steel using laser cladding technology as substitute materials with excellent wear resistance and corrosion resistance, respectively. Subsequently, the phase composition, microstructure, crystallographic texture, microhardness distribution, wear behavior and corrosion behaviour of the two coatings were investigated. The results showed that the iron-based coating mainly composed of α -Fe and Cr_{23}C_6 phases, while the cobalt-based coating mainly composed of γ -Co and Cr_{23}C_6 . There was no obvious texture in the two coatings, and the grain orientation showed a random characteristic. The grain size of iron-based coatings is greatly smaller than that of cobalt-based coatings. The average microhardness of the iron-based and cobalt-based coatings is 704 HV and 502 HV. The simultaneous effect of fine grain strengthening and second phase strengthening ensures high wear resistance of the iron-based coating. The combination of Cr-rich passive film and fine dispersed carbides ensures high corrosion resistance of the cobalt-based coating.

Keywords cobalt-based coating, electrochemical corrosion, iron-based coating, laser cladding, wear property

1. Introduction

From the early 1900s, stainless steel was introduced and has been employed in a wide range of fields because of its good corrosion resistance, high processability, and low cost (Ref 1). One of them, 304 stainless steel is a chromium-nickel stainless steel with austenite as the main structure, which is extensively utilized in the aerospace, chemical, and nuclear power industries because of its outstanding corrosion resistance (Ref 2). However, in some environments containing a large number of chloride ions (such as seawater, and hydrochloric acid), it is easy to occur pitting corrosion, which will lead to material failure, ultimately causing serious financial losses (Ref 3, 4). Therefore, the research on enhancing the corrosion resistance and wear resistance of 304 stainless steel by surface modification technology has received more and more attention.

To elevate the mechanical properties of stainless steel and other alloys for engineering applications, researchers have conducted extensive research on many surface modification

techniques, including welding, thermal spraying, vapor deposition (CVD/PVD), ion implantation, and laser cladding (LC) (Ref 5, 6). Among these, LC is considered the most prospective surface modification technique because of its low dilution rate, low deformation, high bond strength, and dense forming structure (Ref 7, 8). LC is a technique that uses a high-energy laser beam to irradiate a preset or synchronized feed powder and a thin layer over the substrate, quickly melting and solidifying both to form a cladding layer with metallurgical bond to substrate (Ref 9). Thus, the development of various laser cladding wear-resistant and corrosion-resistant alloy coatings has important theoretical significance and engineering application value.

Researchers have developed a variety of LC alloy coatings suitable for different alloys for engineering applications. Wang et al. (Ref 10) prepared in situ synthesized V_8C_7 reinforced iron-based composite coatings by LC on 35CrMo substrates. They investigated in detail the phase evolution and wear resistance of the composite coating. The in-situ generated fine V_8C_7 reinforcing particles significantly improve wear resistance of the coating through second-phase reinforcement, and the hardness was increased to 775 HV. Ding et al. (Ref 11) investigated the influence of adding different contents of VN alloy on the surface properties of cobalt-based LC coatings. The experimental results show that a small amount of VN phase is formed after the addition of the VN alloy, and the percentage of short rod-like dendrites and equiaxed dendrites in the dendritic structure is significantly increased. Compared with cobalt-based coating, the microhardness increased by 12% when adding 5% VN alloy, which significantly improved the wear resistance. In addition, they also carry out aging treatments on cobalt-based composite coatings with the addition of VN. After aging at 750 °C for 3 h, the number of fine equiaxed dendrites in the dendrite structure increased, while the number of long dendritic

F. Jin, S. Zhang, C.L. Wu, and C.H. Zhang, School of Materials Science and Engineering, Shenyang University of Technology, Shenyang 110870 Liaoning, People's Republic of China; X.Y. Sun, Shenyang Dalu Laser Technology CO., Ltd, Shenyang 110136 Liaoning, People's Republic of China; and X.L. Bai, Shenyang Donfon Titanium Industry CO., Ltd, Shenyang 110016 Liaoning, People's Republic of China. Contact e-mails: songzhang_sy@163.com and mfcfclwu@163.com.

dendrites decreased significantly, which further enhanced the composite coating's hardness and wear resistance (Ref 12). Zhu et al. (Ref 13) tempered AISI 420 martensitic stainless steel prepared by LC technology at 210 °C for 1 h. It was found that the martensitic structure decomposed into finely tempered martensite, partially restore to austenite, and the dislocation density was noticeably reduced. The microhardness and tensile strength of the coating are slightly reduced during the tempering treatment, but the toughness is significantly improved and corrosion resistance is not affected. Lu et al. (Ref 14) prepared Fe-based coatings containing Ni-based transition layers on H13 steel substrates by LC technique. And then, the surface of the coating was subjected to massive laser shock peening treatment (MLSP). MLSP introduced a compressive residual stress of 750 μm in depth on the LC coating surface with a value of about 379 MPa, while the high density of dislocations and nano-crystallization caused by plastic deformation also considerably improved the wear resistance of the coating. Wang et al. (Ref 15) prepared LC (CoCrFeNi)₉₅Nb₅ high entropy alloy (HEA) coating on the Q235 steel substrate. When the appropriate laser power is used, the high hardness leaves phase and the high content Cr₂O₃ passivation film make the microhardness and corrosion resistance of the coating significantly higher than the substrate. Wu et al. (Ref 16) prepared LC FeNiCoCrMo_x (x is atomic ratio) HEA coating on 316ss substrate. When the atomic ratio of Mo is 0.20%, the microhardness and corrosion current density of the coating is 447.7 HV and 3.68×10^{-8} A/cm², 1.85 times and 0.77 times of the substrate, respectively. It means that LC FeNiCoCrMo_{0.20} coating significantly improves the wear and corrosion resistance of 316ss stainless steel. In summary, researchers are currently using various methods to obtain high-performance LC coatings, such as adding alloy compounds, and carbides, applying post-treatment techniques and preparing expensive high entropy alloy coatings. However, it seriously limits the further development of LC coatings under the harsh application environment and the need for extensive use of alloys for engineering applications. Therefore, it is necessary to develop easy-to-use wear and corrosion-resistant LC coatings. Meanwhile, it is important to prepare more cost-effective LC coatings for different environments in order to obtain a better service life.

In this paper, iron-based and cobalt-based coatings were prepared on the surface of 304 substrate by LC technology, respectively. Subsequently, the phase composition, microstructure morphologies, and crystallographic characteristics of the two coatings were thoroughly investigated. Meanwhile, the wear and corrosion behavior of the substrate and coatings were investigated by identifying the morphologies and mechanisms after experimental tests. This research dedicated to provide some theoretical references for the preparation of easy-to-use wear and corrosion-resistant LC coatings.

2. Experimental Procedure

2.1 Materials and Laser Cladding Process

In the present work, an AISI 304 stainless steel plate with a dimension of 150 mm × 150 mm × 15 mm was selected as substrate, with a chemical composition of 0.04 wt.% C, 0.67 wt.% Si, 1.35 wt.% Mn, 8.6 wt.% Ni, 18.3 wt.% Cr,

and balanced Fe. Before the LC process, the 304 substrate was smoothed out with 600-grit sandpaper and then cleaned with alcohol. Iron-based alloy and cobalt-based alloy were chosen as cladding powders for the LC process, with particle sizes between 120 and 180 μm and chemical compositions as presented in Table 1. The alloy powder to be used was put in a vacuum drying oven (YZG-5) and dried at 80 °C for 10 h.

The schematic diagram of the LC process is presented in Fig. 1. The cladding experiment was performed out using the TruDiode 3006 system, with a laser beam diameter of 3.6 mm and a wavelength of 1070 nm. The argon is selected as the protective gas with a flow rate of 15 L/min. The optimized processing parameters of LC are as follows: laser power of 2800 W, overlap rate of 50%, scanning speed of 800 mm/min, and pre-placed powder thickness of 2.5 mm. The iron-based and cobalt-based alloy coatings have the same LC process parameters. For clarity, iron-based alloy coating, cobalt-based alloy coating prepared by LC are defined as iron-based coating, cobalt-based coating, respectively.

2.2 Microstructural Characterization

After cladding, the coatings and part of the substrate were cut into blocks measuring 10 mm × 10 mm × 10 mm using a wire electric discharge machine. Block samples were initially ground on a variety of silicon carbide papers (60 # to 2000 #) and polished with a polisher and then cleaned with alcohol to a mirror finish. A D/max2500Pc x-ray diffractometer (Cu-K α target, 40 kV, 30.0 mA) was utilized to identify the phase composition, with the scanning speed and scanning range of 4°/min and 20-90°, respectively. To observe the microstructural morphology in detail, the iron-based and cobalt-based coatings were etched with aqua regia (HCl: HNO₃ = 3:1) and Marble's solution (50 mL HCl + 50 mL H₂O + 10 g CuSO₄), respectively. The cross-section of the coatings was characterized by HAL-100 Zeiss optical microscope (OM) and S-3400N Hitachi scanning electron microscope (SEM), and energy dispersive x-ray spectroscopy (EDS) was utilized to analyze the chemical composition. The Gemini SEM 300 electron backscatter diffraction (EBSD) system was employed to analyze the crystallographic characteristics of the cross-section of the coating.

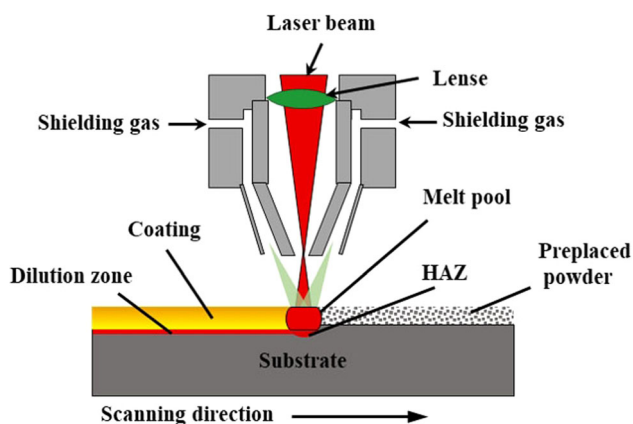
2.3 Microhardness and Sliding Wear Test

In-depth microhardness of all cross sections was measured using the HVS-1000 digital Vickers hardness tester at a load of 2 N and a dwell time of 10 s. The same depth was measured three times at various positions, and an average value and deviation were calculated.

The MFT-400 multi-functional tester was used to evaluate the sliding wear performance of 304 substrate, iron-based and cobalt-based coatings in a reciprocal sliding wear test at room temperature. The process described above uses linear reciprocating friction with ball-on-plate allocation, and 3 mm diameter Si₃N₄ balls are used as the friction pair material. The specimens for the wear test, which were line cutting to a size of 10 mm × 10 mm × 10 mm, were polished to ensure a uniform surface roughness. In the wear test, the sliding speed was 120 mm/min, the load was 15 N, the stroke length was 7 mm and the wear time was 1 h. During the sliding wear test, the friction coefficient was recorded in real time by the wear tester and the wear volume was measured by the Micro XAM-3D white

Table 1 Nominal composition of powder (wt.%)

	C	Cr	Si	Mo	Ni	Fe	Mn	B	W	Co
Iron-based alloy powder	≤ 0.2	16.5	1.15	1.0	1.7	Bal	≤ 0.5	1.25
Cobalt-based alloy powder	1.4	29.0	2.0	1.0	7.0	3.0	8.5	Bal.

**Fig. 1** Schematic diagram of the LC process

light interferometric profiler. The specific wear rate was calculated as:

$$K = \frac{V}{F \cdot L} \quad (\text{Eq 1})$$

where K , V , F and L are the specific wear rate, wear volume, normal load, and sliding route length, respectively.

2.4 Electrochemical Measurement

All electrochemical measurements were performed using a Gamry 600 electrochemical workstation in a 3.5 wt.% NaCl solution at room temperature. The samples for the electrochemical test, which are line cutting to a size of 10 mm × 10 mm × 10 mm, are polished to ensure a uniform surface roughness. The saturated calomel electrode (SCE), the platinum electrode and the specimen were selected as the reference, auxiliary, and working electrodes, respectively. The surface area of the samples used as a working electrode was 1 cm², and the other parts were coated with epoxy resin. Before the electrochemical impedance spectroscopy (EIS) and potentiodynamic polarization (PDP) tests, the samples used as working electrodes were immersed in 3.5 wt.% NaCl for 1800 s open circuit potential (OCP) testing to obtain a steady state, and reference potential. Then, electrochemical impedance spectroscopy (EIS) measured that the voltage amplitude near the OCP was ± 10 mV in the frequency range of 100 kHz to 0.01 Hz. The impedance data were fitted with zsimpwin software. The corrosion potential of the potentiodynamic polarization (PDP) curve is started at − 0.5 V and ended at + 1.0 V, and the voltage scanning rate is 0.5 mV/s. Finally, the corrosion morphology after potentiodynamic polarization was analyzed by SEM images.

3. Results and Discussion

3.1 Phase Composition and Microstructure Analysis

Figure 2 shows the x-ray diffractograms of the surfaces of the iron-based and cobalt-based coatings. The iron-based coating mainly composed of α -Fe and Cr₂₃C₆ phases, while the cobalt-based coating mainly composed of γ -Co and Cr₂₃C₆. As compared to the standard PDF card lines, it is apparent that the diffraction peaks of the matrix phases of both coatings are slightly moved to the left. This may be due to lattice distortion caused by a solid solution of alloying elements into the α -Fe and γ -Co matrix phases and laser-induced thermal stress. Wang et al. (Ref 17) also reported a similar phenomena in their research. In addition, the Cr₂₃C₆ phase was generated in situ in both coatings. Because the bcc structure of α -Fe and the fcc structure of γ -Co have a weak carbon solubilization capacity, excess C and Cr elements tend to form carbides. Moreover, it is critical to analyze the formation mechanism of the carbide phases in the coatings by changes in Gibbs free energy. The following reactions may occur in iron-based and cobalt-based coatings during LC process (Ref 18, 19).



$$\Delta G^0 (\text{kJ/mol}) = -174.401 - 0.0259T (298\text{K} < T < 2171\text{K})$$



$$\Delta G^0 (\text{kJ/mol}) = -309.616 - 0.0774T (298\text{K} < T < 1773\text{K})$$



$$\Delta G^0 (\text{kJ/mol}) = 25.92 - 0.023T (298\text{K} < T < 463\text{K})$$

$$\Delta G^0 (\text{kJ/mol}) = 26.67 - 0.025T (463\text{K} < T < 1115\text{K})$$

$$\Delta G^0 (\text{kJ/mol}) = 10.34 - 0.010T (1115\text{K} < T < 1808\text{K})$$

Where ΔG^0 is the Gibbs free energy and T is the temperature. Figure 3 shows the Gibbs free energy value change curves for Eq 2-4, with temperatures ranging from 300 to 1800 K. At high temperatures, the Gibbs free energy values for the above reactions are all less than 0, which means that all of the above reactions can proceed spontaneously. Compared with Fe₃C and Cr₇C₃, the formation of Cr₂₃C₆ has the lowest Gibbs free energy, so it is easier to form and precipitate prior to other phases in the melt during the solidification process in thermodynamics. This also explains why carbides such as Fe₃C and Cr₇C₃ are not evident in the x-ray diffractograms.

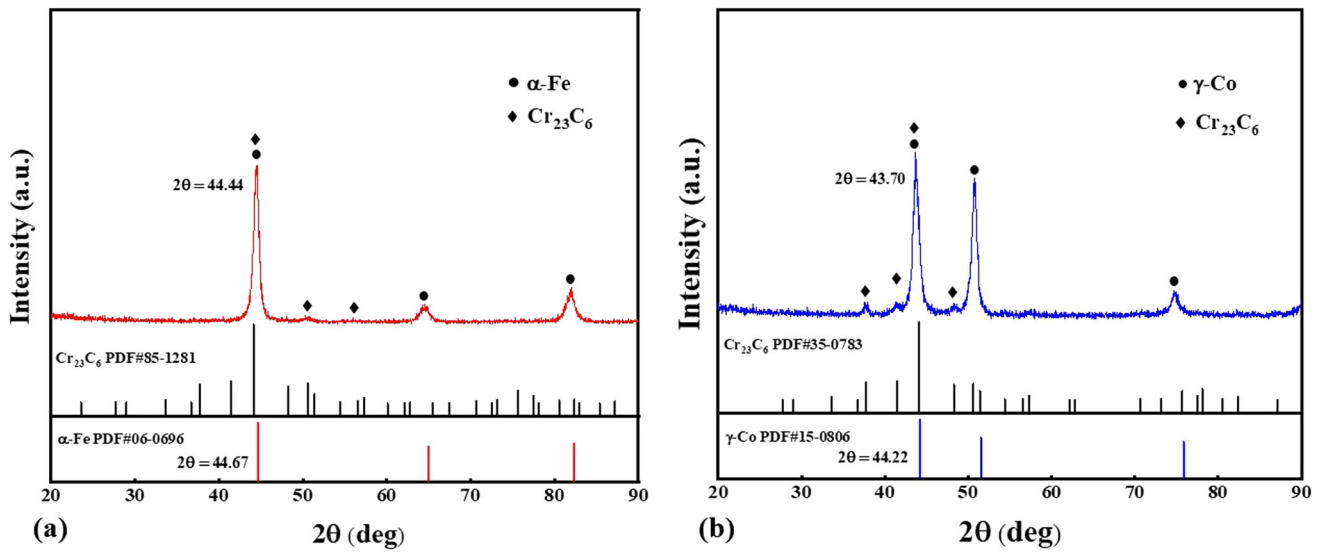


Fig. 2 X-ray diffractograms of (a) iron-based and (b) cobalt-based coatings

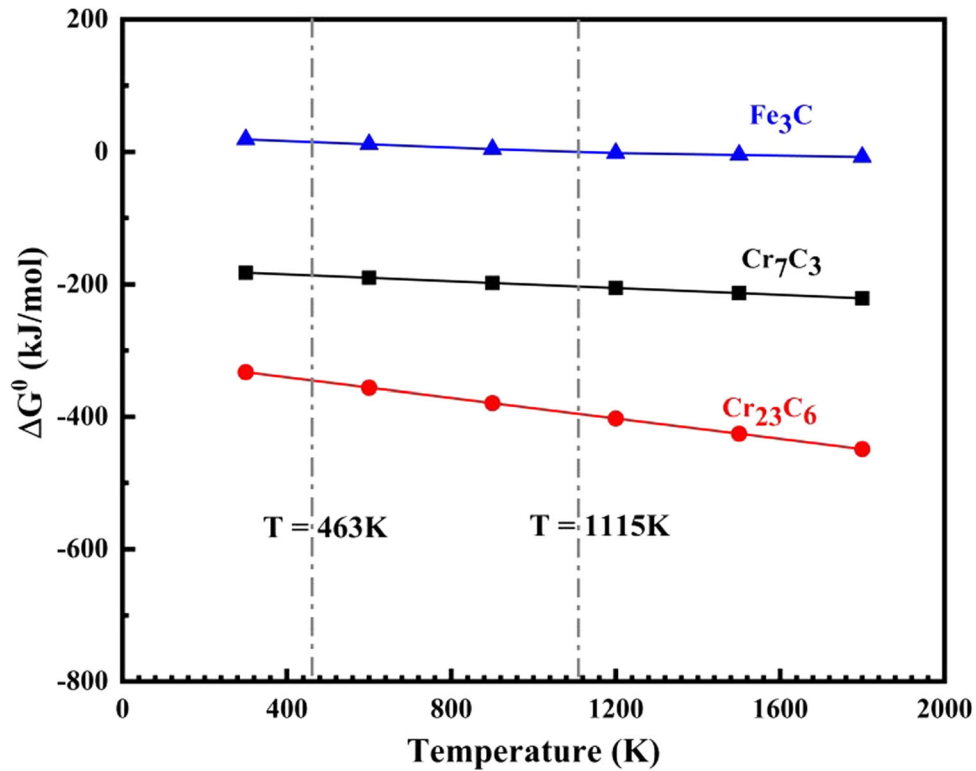


Fig. 3 The changes of the Gibbs free energy ΔG^0 for Cr_7C_3 , $Cr_{23}C_6$ and Fe_3C at different temperatures T

Figure 4(a)–(f) shows typical OM morphologies for different regions of the cross-section of the iron-based and cobalt-based coatings. It is clearly visible that there are no noticeable defects like cracks, holes, porosity and incomplete dissolution within the coating. The interface region of the two coatings is mainly consists of a thin layer of planar crystals, cellular crystals, and columnar dendrite. The columnar dendrites grow in a direction parallel to the temperature gradient G , exhibiting a distinct epitaxial growth feature. The middle region of the coating is mainly consists of dendritic structure and columnar dendrites growing in the direction of the top region. The top

region of the coating consists of a small number of columnar dendrites and dendritic crystals of varying orientation, as well as a large number of equiaxed dendritic structures. The reasons for these phenomena can be explained by the melt pool solidification theory. Figure 5 shows the changes in dendrites structure in the melt pool during LC process. During the solidification of metals, the microstructure is mainly determined by the temperature gradient G and the solidification rate R (Ref 20). It is apparent from the diagram that G/R dictates the solidification structure shape and $G \times R$ dictates the size of the solidification structure. In the LC process, the larger the value

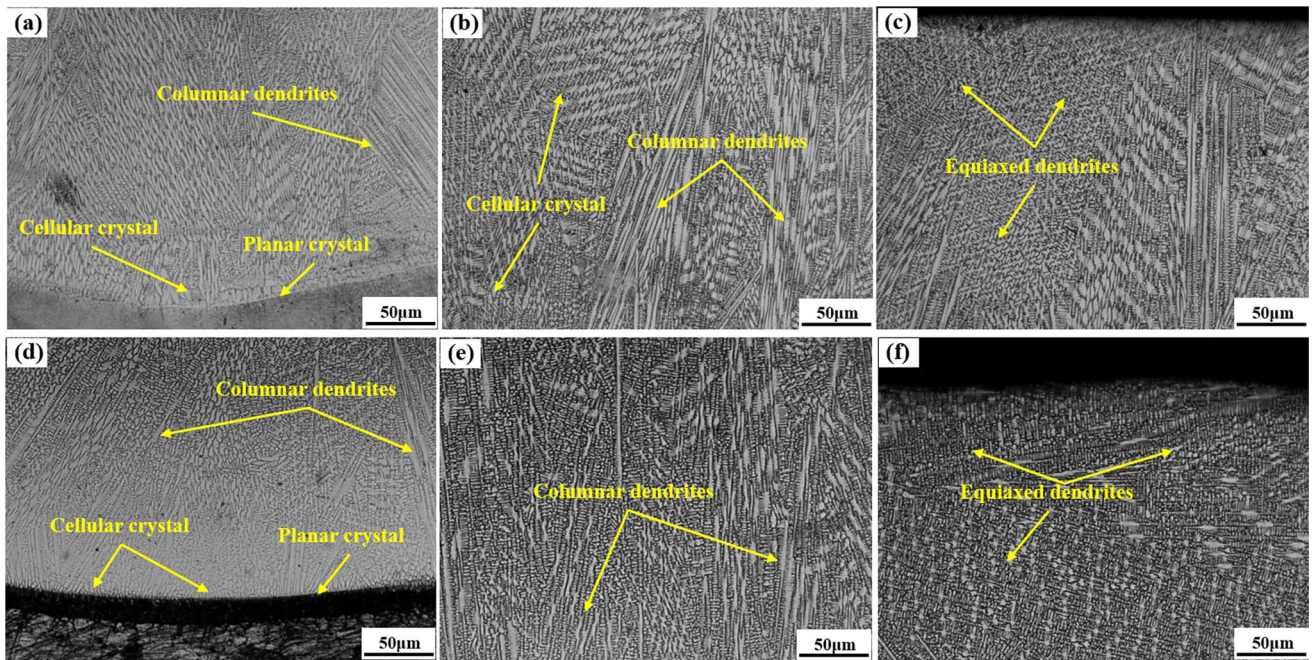


Fig. 4 The typical cross-sectional OM morphologies of iron-based and cobalt-based coatings. (a) the interface region of the iron-based coating, (b) the middle region of the iron-based coating, (c) the top region of the iron-based coating, (d) the interface region of the cobalt-based coating, (e) the middle region of the cobalt-based coating, and (f) the top region of the cobalt-based coating

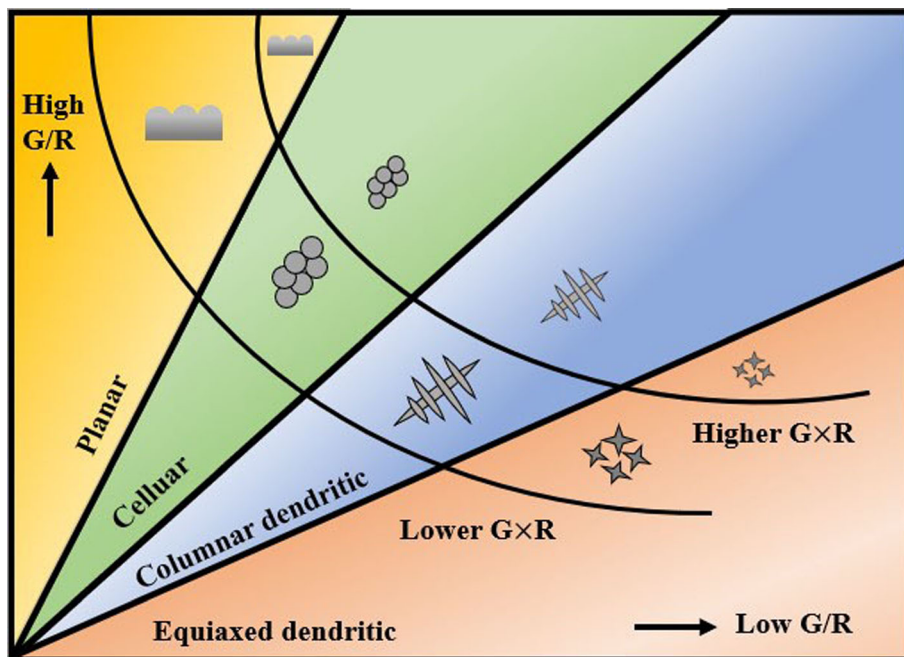


Fig. 5 The changes in dendrites structure in the melt pool during LC process

of $G \times R$, the smaller the size of the solidification structure. As G/R decreases, the solidification structure will gradually form planar crystals, cellular crystals, columnar dendrites, dendrites crystals, and equiaxial dendrites. Compared to iron-based coating, cobalt-based coating have a finer and denser microstructure. It is worth noting that in Fig. 4(d), instead of a bright white band like an iron-based coating, a black transition zone of several microns is visible at the bonding area between cobalt-based coating and 304 substrate. This is owing

to the fact that the high-energy laser beam melts the cobalt-based alloy powder and the 304 substrate, a transition zone is formed due to the greater diffusion of elements between the substrate and the coating (Ref 21).

To observe the phase and microstructural characteristics in detail, the typical cross-sectional SEM morphologies of the top region of the iron-based and cobalt-based coatings are shown in Fig. 6. According to Fig. 6(a) and (c) the microstructure of the iron-based and cobalt-based coatings is characterized by a

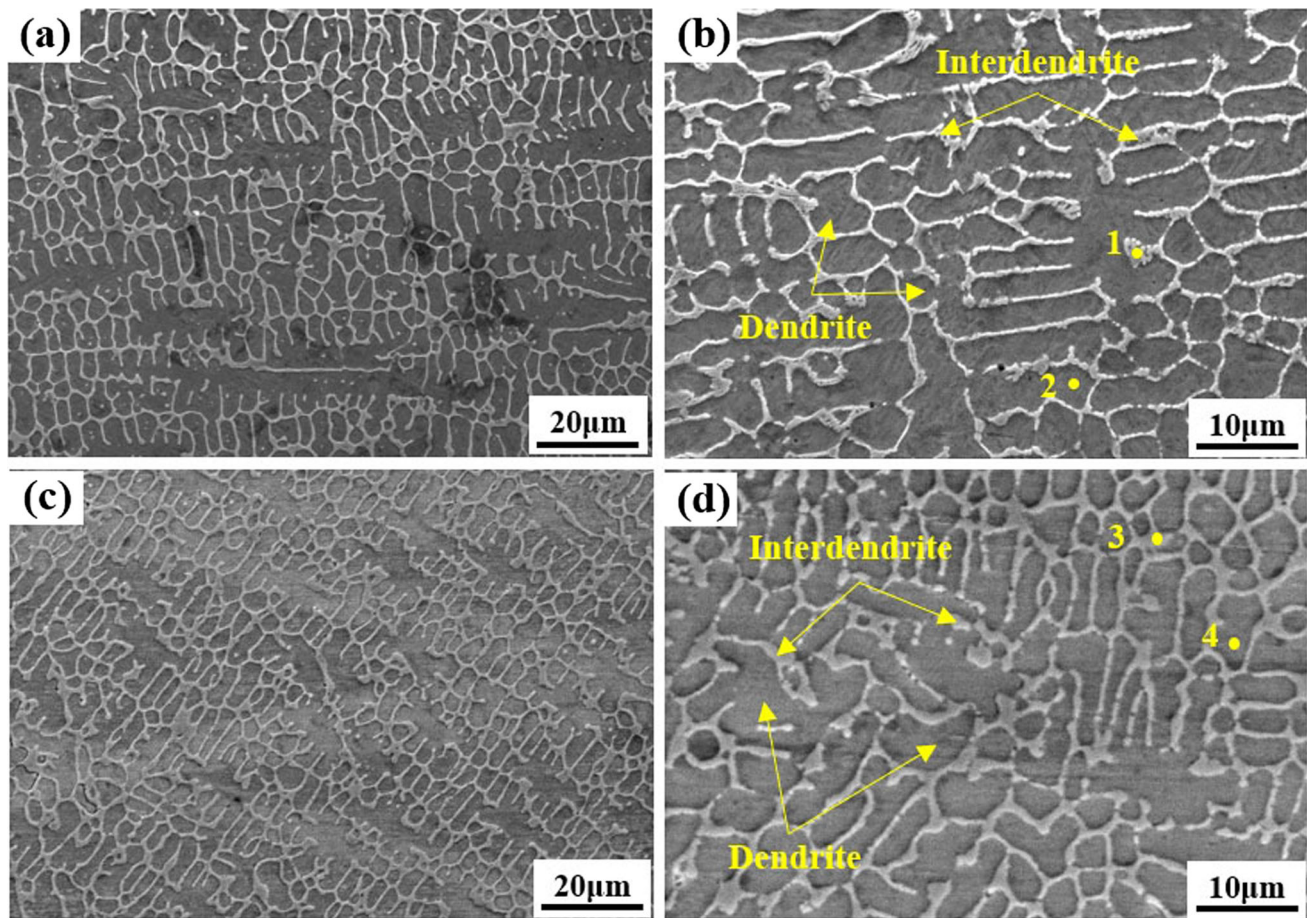


Fig. 6 The typical cross-sectional SEM morphologies of iron-based and cobalt-based coatings. the top region of the iron-based coating (a) low magnification, and (b) high magnification; the top region of the cobalt-based coating (c) low magnification, and (d) high magnification

eutectic structure (dendrites and interdendrites mixed structure), which exhibits typical rapid solidification characteristics. During the cooling of the cladding layer, the dendrites first nucleate from the melt pool and continuously grow into the dendritic matrix. During cooling and solidification, the intercrystalline metal solution undergoes eutectic reactions, resulting in an intercrystalline reticulated eutectic structure. It can be seen that the microstructure of the cobalt-based coating is finer and denser than that of the iron-based coating, which corresponds to the OM images. Wang et al. (Ref 22) investigated the influence of different contents of Mo on iron-based coatings, showing that the introduction of Mo elements reduced the size of carbide particles and improved intercrystalline stability and continuity. Therefore, the introduction of the Mo element encourages the forming of thin interdendrites structures in the iron-based coating. The results of the research by Yang et al. (Ref 23) show that as the thermal conductivity of Ni ($0.22 \text{ J}/(\text{cm s } ^\circ\text{C})$) is higher than that of Fe ($0.18 \text{ J}/(\text{cm s } ^\circ\text{C})$), the increase in Ni promotes the separation of dendrites from interdendrites elements and accelerates the solidification rate, thereby promoting the formation of fine eutectic structures. Cobalt-based coatings have a higher content of Ni, which facilitates the formation of a finer microstructure.

To understand the distribution of elements in the dendrites and interdendrites region of the two coatings, an EDS point analysis on points 1-4 in Fig. 6 were performed and the results are shown in Table 2. For iron-based coatings, the dendrites

have a higher Fe and Ni content than the interdendrites structure, and the interdendrites structure have a higher C, Cr and Mo element content than the dendrites. Combined with the XRD results, it is possible to speculate that the dendrites are mainly consisted of the α -Fe phase, with interdendritic Cr and C elements gathering to form carbide phases such as Cr_{23}C_6 and Cr_7C_3 . For the cobalt-based coating, Co, Fe, Ni elements are widely distributed in the coating, with more in the dendrites to form the matrix phase. Cr, C, Mo, and W elements are widely distributed in the coating, but they are more likely to gather among interdendrites to form the carbide phase. Combined with the XRD results, it is conceivable to deduce that the dendritic matrix of the cobalt-based coating is mainly consist of γ -Co and its solid solution phase, and the network-like interdendrites are high hardness Cr_{23}C_6 , Cr_7C_3 , and other carbides. The research results of Ma et al. (Ref 24) show that the distribution of Cr_{23}C_6 carbides between the dendrites inhibits dislocation movement, improves the bonding strength between the melt layers, and relieves convection within the melting pool, which is essential for the overall performance of the coating. In addition, W, Cr and Mo elements can be replaced with the matrix Co and Fe to form a solid solution, resulting in solid solution strengthening effect. It should be noted that the Fe content of the cobalt-based coating is significantly higher than that of the cobalt-based alloy powder, which confirms once again that significant interdiffusion occurs between the substrate and the coating.

Table 2 EDS analysis of the different positions in Fig. 6 (wt.%)

Point	C	Cr	Mo	Si	Ni	Fe	Mn	Co	W
1	1.75	16.90	2.66	0.46	1.01	76.79	0.42
2	1.20	11.29	0.66	0.60	1.28	84.60	0.37
3	2.41	33.60	4.86	2.67	5.77	16.55	...	23.40	10.74
4	2.07	19.22	1.06	1.74	11.58	25.89	...	32.93	5.51

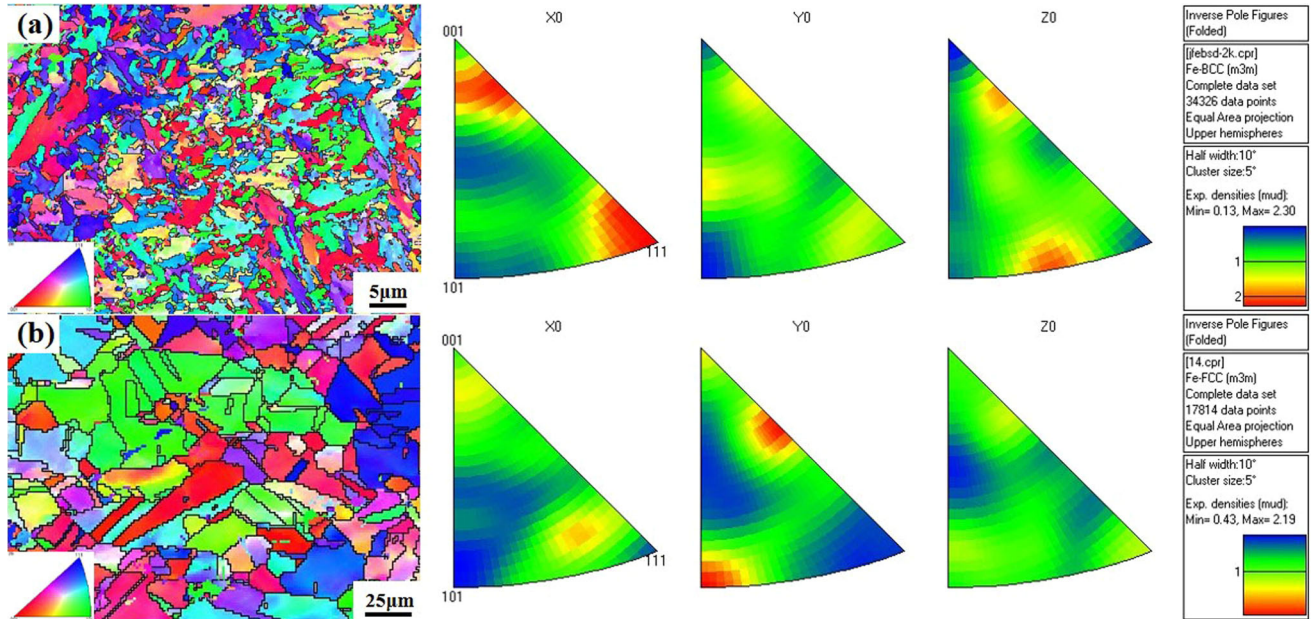


Fig. 7 The cross-sectional EBSD orientation maps and inverse pole figures. (a) iron-based coating; (b) cobalt-based coating

3.2 Crystallographic Characterization and Microhardness Distribution

To explore the preferential growth orientation of the grains, average grain size, and the related crystallographic characteristics, the top region of the coating's cross-section was further characterized by EBSD. In this paper, to express the experimental results more clearly, different magnifications were used for each of the two coatings when carrying out EBSD analysis, which did not affect the experimental results. The cross-sectional EBSD orientation maps and corresponding inverse pole figures for the top region of two coatings are shown in Fig. 7. The blue, red, and green colors in the EBSD orientation maps reflect the $\langle 111 \rangle$, $\langle 001 \rangle$, and $\langle 101 \rangle$ grain orientations, and the rest of the colors represent the middle orientations. The textural intensity of the iron-based and cobalt-based coatings is 2.30 and 2.19, respectively. There is no obvious texture in the two coatings and the grain orientation shows a random characteristic. This phenomenon can be attributed to the inherent characteristics of the solidification structure during the LC process. Texture formation is primarily influenced by the direction of heat transmission and the local temperature gradient (Ref 25). However, in the top region of the cladding layer, the G/R is small, while disordered grains form near the surface because of the stirring effect of the laser beam. At this point, substrate heat dissipation no longer plays a

dominant role and the grain orientation is mainly determined by crystallographic anisotropy, so no distinct texture is occurred (Ref 26). Meanwhile, it is observable that the grain size of the iron-based coating is considerably finer than that of the cobalt-based coating.

In-depth microhardness distributions in iron-based and cobalt-based coatings is illustrated in Fig. 8. The iron-based and cobalt-based coatings had an average microhardness of 704 HV and 502 HV, respectively, that is about 3.8 and 2.7 times that of the substrate. In addition, an increase in microhardness in the heat-affected zone can be noticed, which is attributed to the quenching effect of the laser energy on the substrate (Ref 27). In this paper, the two cladding layers possess a high degree of microhardness, there may be two main reasons: one is solid solution strengthening caused by solute atoms entering the α -Fe matrix and the γ -Co matrix to induce lattice distortion and enhance the resistance to dislocation movement; the other is the second phase strengthening caused by the high hard phases Cr_{23}C_6 and Cr_7C_3 dispersed in the network like interdendrites region. However, for iron-based coatings, it is necessary to consider the fine grain strengthening caused by small grain sizes (Ref 28). The relationship between the strength of a material and grain size is defined by the Hall-Petch relationship, which can be described as below:

$$\sigma_y = \sigma_0 + kd^{-\frac{1}{2}} \quad (\text{Eq 6})$$

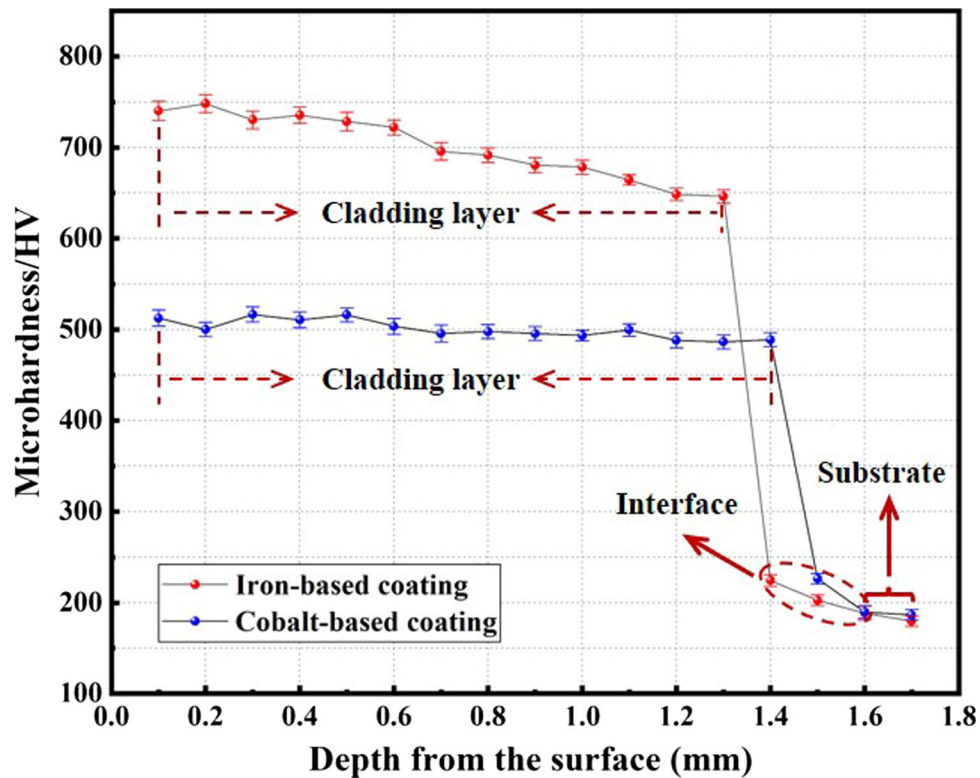


Fig. 8 In-depth microhardness distributions in iron-based and cobalt-based coatings

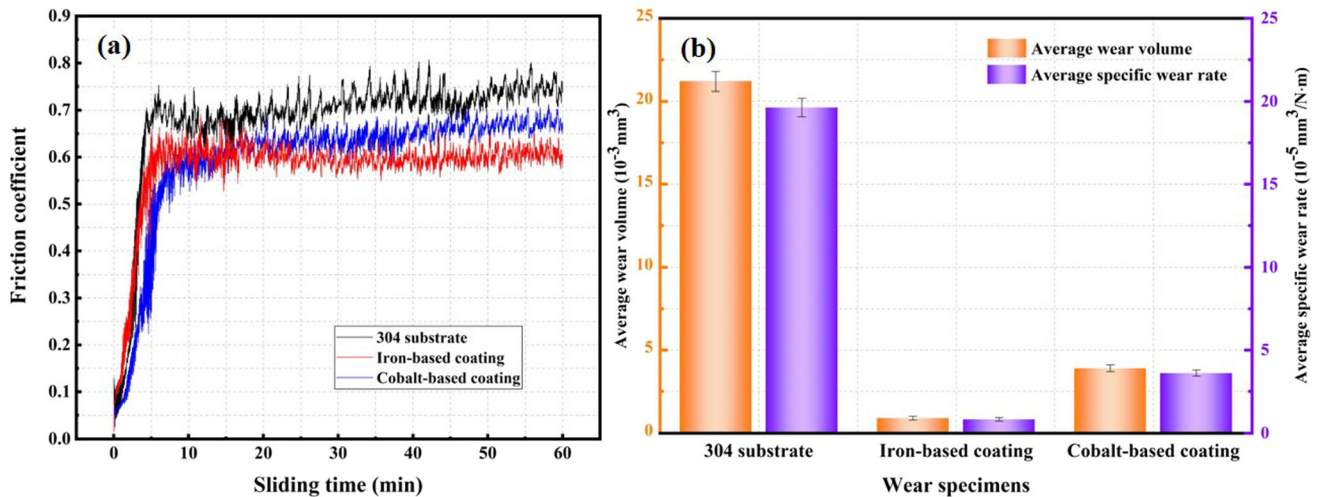


Fig. 9 (a) Friction coefficient curves, wear volume and (b) specific wear rate of 304 substrate, iron-based and cobalt-based coatings

where σ_y is the yield strength, σ_0 is the constant stress of materials, k is the Hall-Petch constant and d is the average grain diameter. According to Eq (6), it can be speculated that the smaller the grain size, the higher the microhardness (Ref 29). This is why the iron-based coating has a comparable microhardness to the WC-reinforced iron-based coating (Ref 30).

3.3 Wear Behavior

The friction coefficient is one of the key parameters in the assessment of friction and wear performance. In general, under uniform wear conditions, a lower friction coefficient means that

the material has excellent wear properties. Fig. 9(a) shows the average friction coefficient of 304 substrate, iron-based and cobalt-based coatings, which are 0.682, 0.579 and 0.597, respectively. Both cladding coatings have a lower average friction coefficient than the substrate, implying a better wear resistance. The friction coefficient of the cobalt-based coating is slightly lower than that of the iron-based coating for durations from 0 to 15 min. After this period, the friction coefficient of the iron-based coating is significantly lower than that of the cobalt-based coating, which means that the iron-based coating has better wear resistance.

To further explore the wear performance, the wear volume and specific wear rate of the 304 substrate, iron-based, and cobalt-based coatings were calculated and displayed in Fig. 9(b). The average wear volume of the 304 substrate, iron-based, and cobalt-based coatings are $21.2 \times 10^{-3} \text{ mm}^3$, $0.9 \times 10^{-3} \text{ mm}^3$ and $3.9 \times 10^{-3} \text{ mm}^3$ respectively, while the average specific wear rate are $19.63 \times 10^{-5} \text{ mm}^3/\text{N m}$, $0.83 \times 10^{-5} \text{ mm}^3/\text{N m}$, and $3.61 \times 10^{-5} \text{ mm}^3/\text{N m}$, respectively. Compared with 304 substrate, the specific wear rate of two coatings are decreased by 95.8% and 81.6%, showing a better wear resistance. Particularly, iron-based coating shows a lower wear rate than that of cobalt-based coating, which is aligned with the consequences of friction coefficient in Fig. 9(a).

To understand the wear mechanisms of the 304 substrate, iron-based and cobalt-based coatings, SEM images and EDS analyses of worn surfaces were performed, as shown in Fig. 10. Severe wear damage appeared on the 304 substrate surface, as present in Fig. 10(a), including characteristics of spalling pits, delamination, cracks, wear debris and extensive plastic deformation. Because of the low hardness of the 304 substrate, cracks are initiated and extended too early under normal and tangential forces, and then these cracks combine together to cause remarkable deformation and spalling on the worn surface (Ref 31). Additionally, based on the EDS analysis in Fig. 10(d), large oxide patches were found on the worn surface, which emphasizes the experience of oxidative wear during the wear process. The frictional heat caused by cyclic sliding loads promotes the occurrence of loose oxide layers, which tend to peel off under contact stress (Ref 32). Thus, the main wear mechanism of the 304 substrate is adhesive wear and oxidative wear.

As illustrated in Fig. 10(b) and (c), worn damage is significantly weaker for iron-based and cobalt-based coatings. For cobalt-based coatings, there is no deformation or extensive spalling, but there are the width and deep grooves and a small number of cracks and delamination on the worn surface. Under dry sliding wear conditions, the material is peeled off the

surface under sliding pressure in the form of smaller wear debris and particles, and then the abrasive material is embedded in the soft surface under normal forces and scratches deep grooves in the surface under shear loading. According to the EDS analysis in Fig. 10(f), the reaction between the metal atoms and the O atoms causes local oxidation, and the oxide easily sticks to the friction pair and then peels off from the surface of cobalt-based coating. Such phenomena indicate that the wear mechanism of cobalt-based coatings consists of abrasive wear accompanied with a certain degree of adhesive wear and oxidative wear. In contrast, the wear surface of iron-based coating is relatively smooth, with only a few shallow grooves and slight spalling, and the results of the EDS analysis in Fig. 10(e) show that no oxidative wear has occurred. Therefore, the wear mechanism of iron-based coatings is abrasive wear accompanied with a slight adhesive wear. The good wear resistance of the iron-based and cobalt-based coatings is mainly due to the formation of dense dendrites and the second phase reinforcement caused by the high hardness carbides.

Figure 11 presents a schematic diagram of the wear damage mechanism for iron-based and cobalt-based coatings. During the wear process, the cyclic load leads to work hardening and forms a high hardness tribo-layer on the surface of the worn track (Ref 33). It separates the counter ball from the bottom layer to avoid direct contact of friction pairs. For iron-based coatings, during the sliding wear process, a dense tribo-layer is formed on the surface, resulting in small grooves and a small amount of wear debris. However, the tribo-layer formed on the surface of the cobalt-based coating is weaker, resulting in distinct deep grooves and large pieces of wear debris. Iron-based coatings have superior wear resistance than cobalt-based coatings, which is attributable to grain boundary strengthening and high microhardness. Zhou et al. (Ref 34) reported that high density grain boundaries can significantly improve the toughness of steel, which effectively prevents the development of cracks. Furthermore, the microhardness of the material is a key

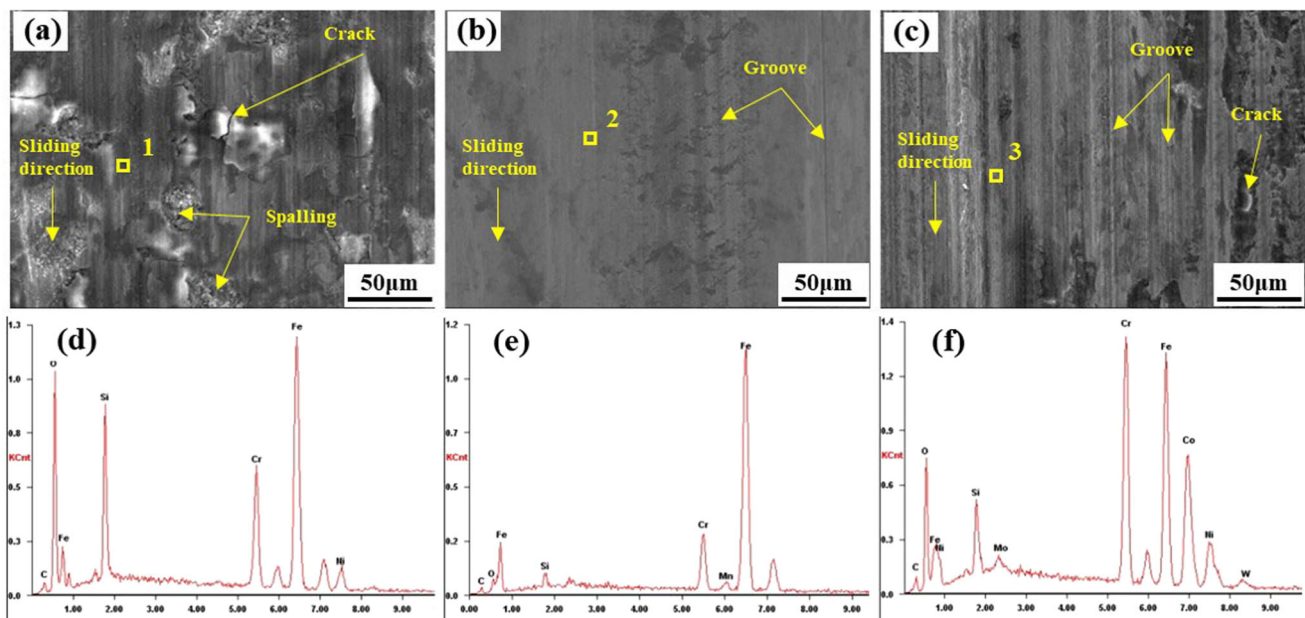


Fig. 10 Typical SEM morphologies and EDS analysis of the worn surface. (a) 304 substrate, (b) iron-based coating, (c) cobalt-based coating, (d) EDS analysis of Point 1, (e) EDS analysis of Point 2, and (f) EDS analysis of Point 3

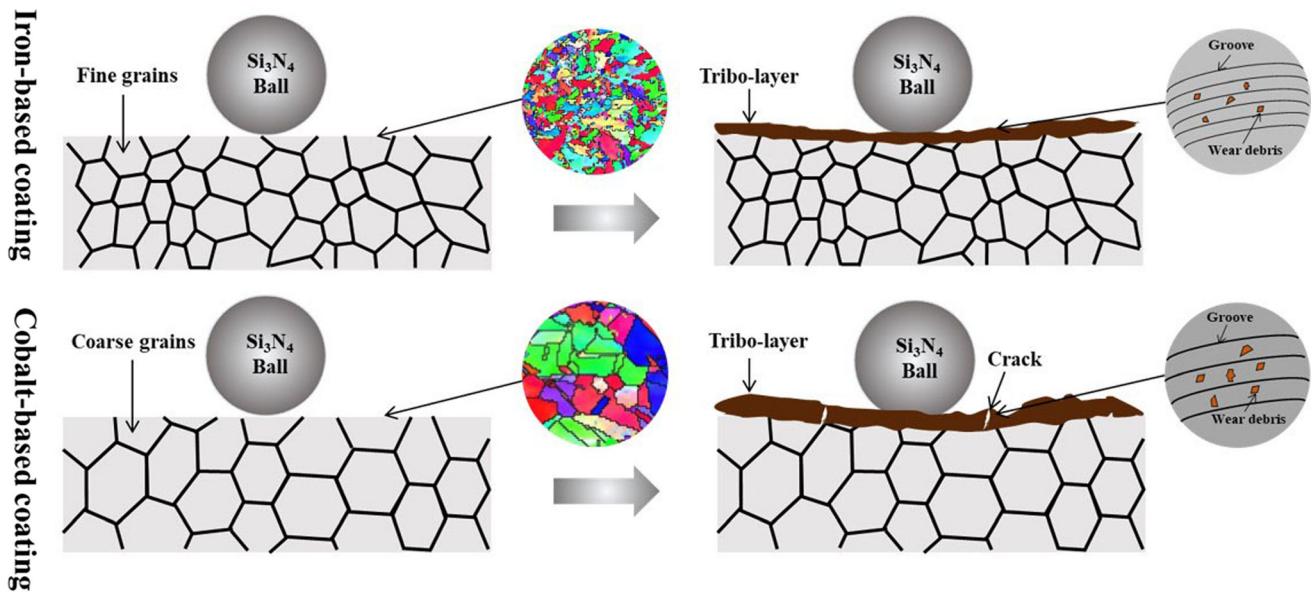


Fig. 11 Schematic diagram of the wear damage mechanism of the iron-based and cobalt-based coatings

factor in determining the wear resistance. The relationship between wear resistance and microhardness is defined by the Archard's law, which can be expressed as below (Ref 35):

$$V = K \frac{P \cdot L}{HV} \quad (\text{Eq 7})$$

where V is the wear volume, K is the wear factor as a constant, P is the positive load, L is the sliding distance and HV is the overall hardness of the coating. According to Eq (7), V decreases as HV increases. The high hardness tends to increase the resistance of the material to plastic deformation and adhesive wear, thereby reducing the molecular adhesion and shearing effects between friction pairs.

3.4 Corrosion Behavior

The corrosion resistance of the different samples is tested by potentiodynamic polarization in 3.5 wt.% NaCl solution. Figure 12 presents the potentiodynamic polarization curves for the 304 substrate, iron-based and cobalt-based coatings. The electrochemical parameters calculated from the polarization curves by using the Tafel extrapolation method, including corrosion potential (E_{corr}) and corrosion current density (I_{corr}), are presented in Table 3. According to Fig. 12 and Table 3, the E_{corr} of the 304 substrate, iron-based and cobalt-based coatings, was -261.52 , -361.75 and -237.26 mV, respectively, and the I_{corr} was 1.653×10^{-7} , 4.570×10^{-7} and 8.911×10^{-8} A cm^{-2} , respectively. It is clear that the cobalt-based coating has the highest E_{corr} and the lowest I_{corr} compared with 304 substrate and iron-based coating. The E_{corr} and I_{corr} indicate the thermodynamic stability and corrosion kinetics of the material, respectively (Ref 36). Generally, the more positive E_{corr} and the lower I_{corr} mean a lower probability of corrosion. Therefore, according to E_{corr} and I_{corr} values, the cobalt-based coating has the lowest corrosion rate, which significantly improves the corrosion resistance of the 304 substrate. Moreover, as demonstrated in Fig. 12, for 304 substrates and iron-based coatings, the passivation zone is not obvious and the passivation film is easily destroyed, resulting in the electrolyte

easily being in contact with the surface of the material to form pitting corrosion (Ref 37). In contrast, cobalt-based coatings have a distinct passivation zone at -261 to -40.53 mV, meaning that a stable passivation film is generated, which can effectively prevent the occurrence of pitting corrosion.

Figure 13 presents the EIS diagrams for the 304 substrate, iron-based and cobalt-based coatings. As shown in Fig. 13(a) and (b), the maximal value of impedance modulus ($|Z|$) and phase angle of the cobalt-based coating are both higher than that of the 304 substrate and the iron-based coating. Generally, the larger the ($|Z|$) value and phase angle corresponds the more stable the passive film and the better the resistance to electrochemical corrosion (Ref 38). As shown in Fig. 13(c), the Nyquist plots for the 304 substrate, iron-based, and cobalt-based coatings are all unfinished capacitive arcs, which indicate a similar corrosion mechanism for the different samples. The larger the radius of the capacitive arc, the better the resistance to pitting corrosion (Ref 39). Obviously, the cobalt-based coating has the largest capacitive arc radius, while the iron-based coating has the lowest capacitive arc radius. In conclusion, the cobalt-based coating has a relatively excellent corrosion resistance, which is in line with the measurement results of the electrochemical corrosion polarization curve.

To better obtain the corrosion features of the different samples, the R(Q(R(QR))) equivalent circuit (Fig. 13(d)) was chosen to fit the EIS results. Within the circuit, R_s , R_b , and R_{ct} are the solution resistance, the passive film resistance and the charge transfer resistance, respectively. To prevent effects caused by nonuniform electrode interfaces, the constant phase element Q is applied instead of the ideal capacitor. Z_Q is Q impedance, that can be defined as below (Ref 40):

$$Z_Q = \frac{1}{K(\omega \cdot i)^{-n}} \quad (\text{Eq 8})$$

where K is the capacitance parameter, i is the imaginary unit, ω is the angular frequency and n is the dispersion coefficient, which demonstrates the deviation of the surface inhomogeneity. The result for the fitting dates are presented in Table 4. The chi-square is a parameter for assessing statistical error. A chi-square

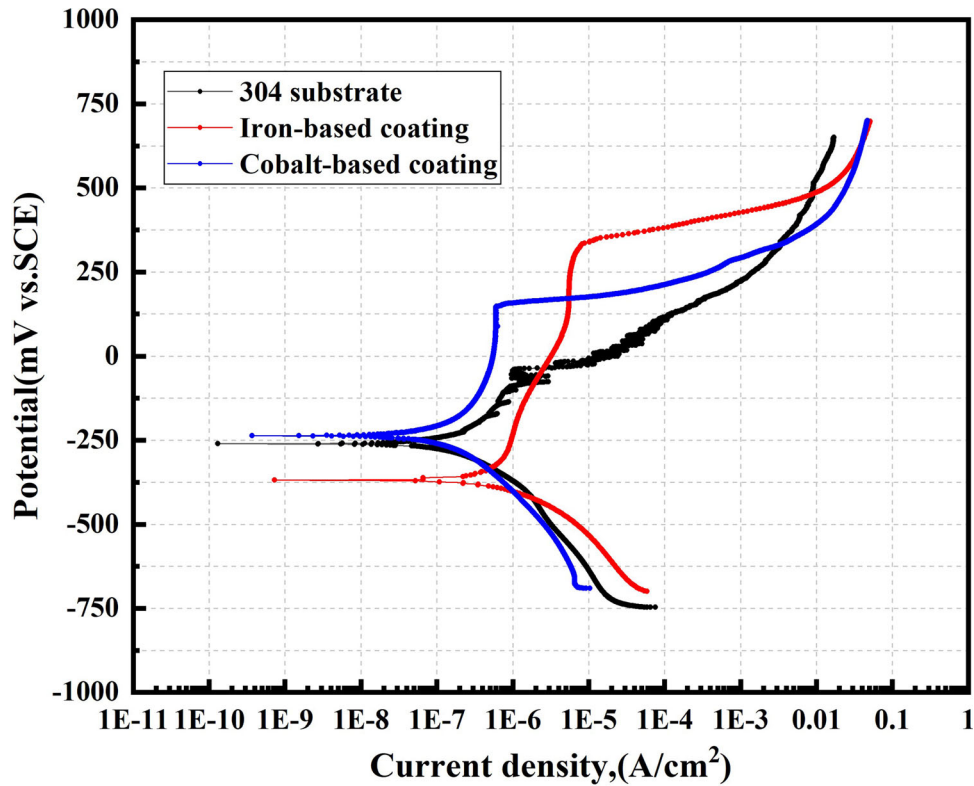


Fig. 12 Electrochemical corrosion polarization curve of the 304 substrate, iron-based, and cobalt-based coatings

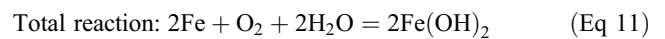
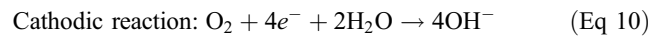
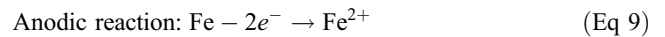
Table 3 Electrochemical parameters determined based on potentiodynamic curves

Sample	E_{corr} , mV	I_{corr} , A cm^{-2}
304 substrate	-261.52	1.653×10^{-7}
Iron-based coating	-361.75	4.570×10^{-7}
Cobalt-based coating	-237.26	8.911×10^{-8}

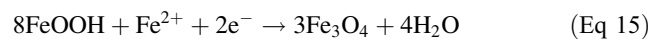
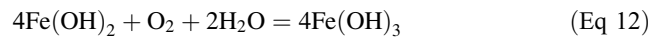
of samples in the range of 10^{-4} to 10^{-5} indicates that the equivalent circuit was fitting closely to the actual situation. The R_b value can be used to assess the stability and density of the passive film, with a higher value meaning better passivation performance (Ref 38). Cobalt-based coatings have relatively higher R_b values, meaning that the passive film formed is thick and stable. The parameters of R_{ct} are closely related to corrosion behavior, the higher the value of R_{ct} , the slower the charge transfer, resulting in a lower corrosion rate of the materials (Ref 41). The R_{ct} value for the cobalt-based coating is $3.436 \times 10^5 \Omega \text{ cm}^2$, which is 2.65 and 4.78 times higher than the 304 substrate and the iron-based coating, respectively, meaning that the electron in cobalt-based coating was more difficult to move. All these EIS analyses show the same pattern as the potentiodynamic polarization analysis.

Figure 14 schematically illustrates the mechanism of the electrochemical corrosion behavior of the LC samples in a 3.5 wt.% NaCl solution. Firstly, the electrolyte cannot react directly when it contacts the surface of the samples. This could be attributed to the fact that the Cr element in the coating will promote the formation of passive films and the anode material state will change from an active to a passive state. However, as

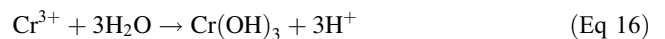
the potential slowly increases, the passivated film on the sample surface is destructed by the chloride ions in the electrolyte, and then anodic reactions occur along with the erosion of the coating. Furthermore, during the anodic reaction, the metal in the coating is oxidized to ions and forms pits and corrosion products. Due to the near neutral pH of the electrolyte, the following electrochemical reactions may occur:



As the reaction continues, $\text{Fe}(\text{OH})_2$ is converted to FeOOH and Fe_3O_4 due to its relatively unstable nature in the electrolyte, and the corresponding equilibrium reactions are as follows:



When the content of the Cr element is high, it is easy to form Cr_2O_3 passivation film, which reaction is as follows:



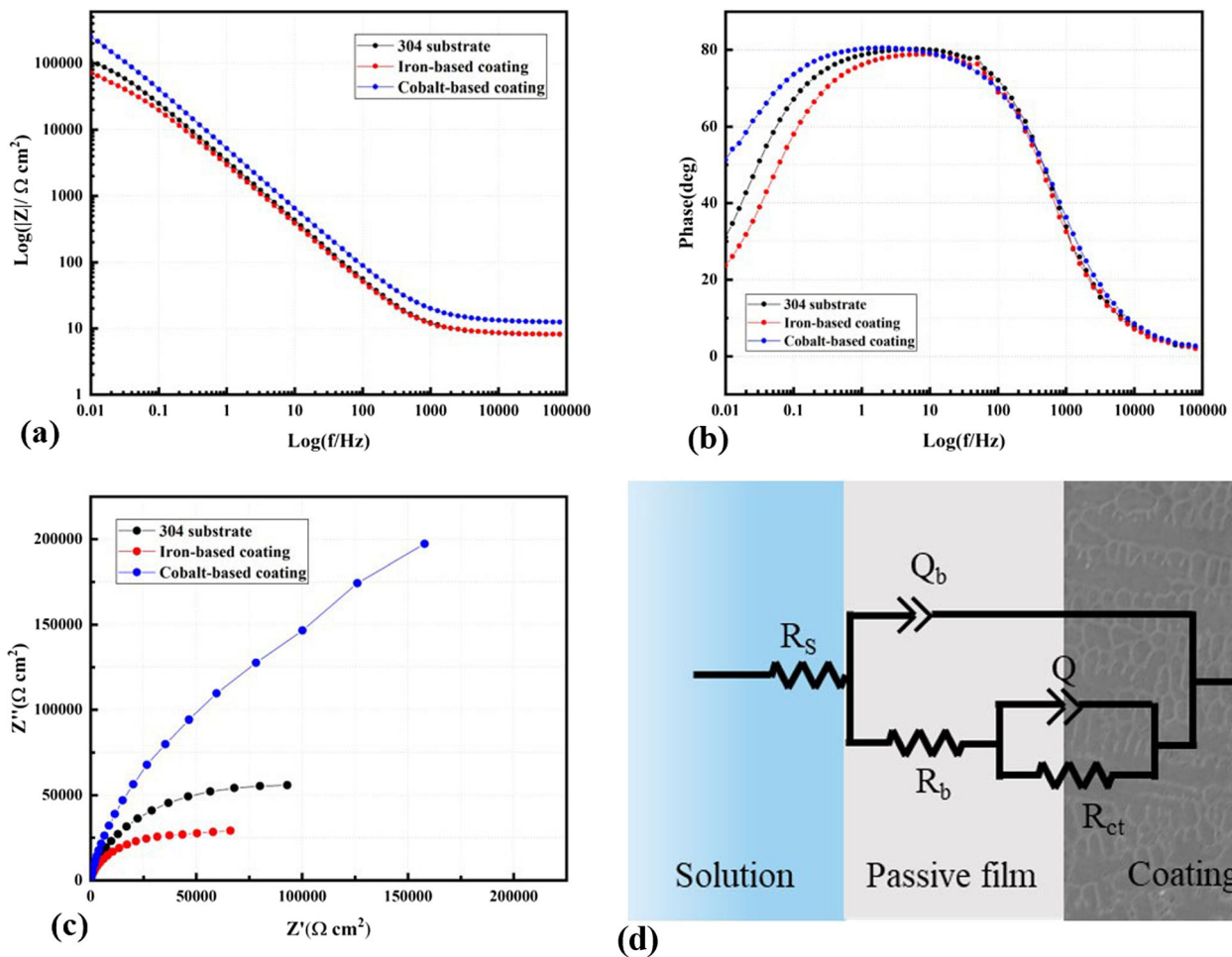


Fig. 13 Electrochemical characteristics of different samples: (a) bode plots; (b) bode phase plots; (c) Nyquist plots, and (d) equivalent electrical circuit model

Table 4 Fitting values of EIS data in the equivalent electrical circuit

Sample	$R_s/\Omega \text{ cm}^2$	$Q_b/\Omega^{-1} \text{ s}^{-n} \text{ cm}^{-2}$	n_b	$R_b/\Omega \text{ cm}^2$	$Q/\Omega^{-1} \text{ s}^{-n} \text{ cm}^{-2}$	n	$R_{ct}/\Omega \text{ cm}^2$	Chi-squared
304 substrate	8.22	1.172×10^{-5}	0.975	4.126	4.557×10^{-5}	0.859	1.299×10^5	3.93×10^{-4}
Iron-based coating	8.28	1.388×10^{-5}	0.870	4.955	5.374×10^{-5}	0.840	7.188×10^4	1.96×10^{-4}
Cobalt-based coating	12.87	1.475×10^{-5}	0.915	8.313	1.628×10^{-5}	0.853	3.436×10^5	7.12×10^{-4}

Figure 15 shows the typical corrosion morphology of iron-based coating and cobalt-based coating after potentiodynamic polarization test. There are many white particles on the corrosion surface of the sample, which is NaCl left on the surface after the polarization test. As can be seen in Fig. 15(a), coarse streaks of corrosion areas and pits appear on the surface of the iron-based coating. It can be noted that the pitting starts preferentially edge of interdendritic region and gradually extends to dendrites region, eventually leading to spalling of the dendrites and leaving a network-like interdendritic structure (Fig. 15b). This is owing to the higher Cr content in the interdendritic region than in the dendritic region, where the Cr atoms promote the formation of Cr_2O_3 oxide films, which improves the corrosion resistance of the interdendritic region (Ref 42). From Fig. 15(c), it is apparent that the area of corrosion pits occurred on the surface of the cobalt-based

coating is smaller and shallower in depth compared to the iron-based coating. It can be noticed that the corrosion still starts in the interdendritic region (Fig15(d)), but dissimilar with the iron-based coating, most of the corrosion products remain on the surface of the coating. According to the research of Gan et al. (Ref 43), high content of Cr and Co elements is contributing to forming a dense passive film, which effectively preventing the continued damage by chloride ions. In addition, the research by Xu et al. pointed out that the fine interdendritic structure plays an important role in the formation of a continuous passivation film with few defects (Ref 44). This enables the cobalt-based coating to form a highly adhesive Cr-rich passivation film at the initial stage of corrosion, which effectively reducing the corrosion rate of coating.

Additionally, it is obvious that the corrosion of both coatings occurs mainly in the interdendritic region, which is a typical intergranular corrosion. The major reason of intergranular

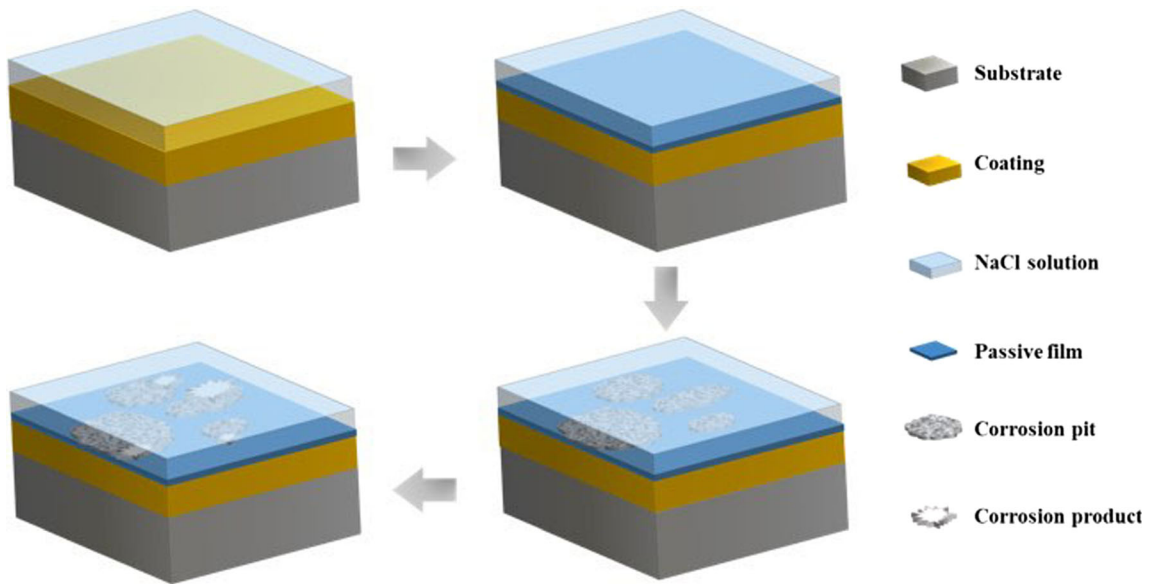


Fig. 14 Schematic diagram of the electrochemical corrosion behavior of laser cladding samples in 3.5 wt.% NaCl solution

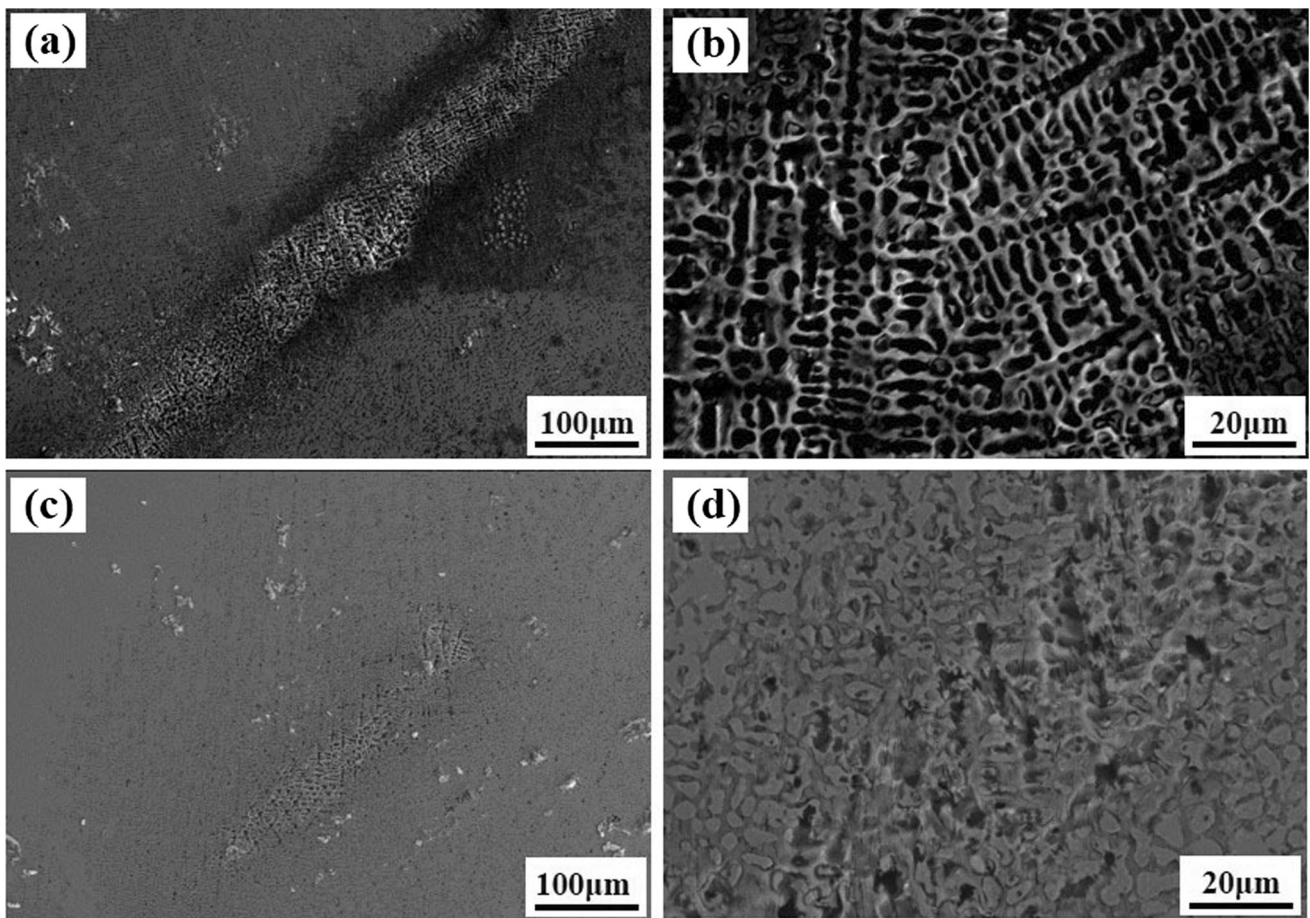


Fig. 15 Typical SEM images of the corroded surface after the electrochemical corrosion experiment. the corrosion morphologies of the iron-based coating (a) low magnification, and (b) high magnification; the corrosion morphologies of the cobalt-based coating (c) low magnification, and (d) high magnification

corrosion is that Cr atoms diffuse rapidly along the grain boundary and form carbides with C atoms, causing a reduction in Cr atoms content near the grain boundary. As a result, the

corrosion property of the interdendritic boundaries declines and preferential corrosion occurs, forming an intergranular corrosion morphologies (Ref 42).

4. Conclusion

- (1) An iron-based and cobalt-based coating with no obvious cracks and holes was successfully prepared on the surface of AISI 304 stainless steel by LC technology. The microstructure of both coatings presented the same growth pattern, with a change from cellular dendrites or columnar dendrites to equiaxed dendrites. The iron-based coating mainly consisted of α -Fe matrix phase and Cr_{23}C_6 phases, while the cobalt-based coating mainly consisted of γ -Co matrix phase and Cr_{23}C_6 phases.
- (2) The EBSD results exhibited that there was no obvious texture of the two coatings and the grain orientation showed a random characteristic. The grain size of iron-based coatings is considerably smaller than that of cobalt-based coatings. The average microhardness of the iron-based and cobalt-based coatings was 704 HV and 502 HV.
- (3) The specific wear rates of the iron-based and cobalt-based coatings were $0.83 \times 10^{-5} \text{ mm}^3/\text{N m}$ and $3.61 \times 10^{-5} \text{ mm}^3/\text{N m}$, respectively. The simultaneous effect of fine grain strengthening and second phase strengthening ensures high wear resistance of the iron-based coating.
- (4) The corrosion current density of the iron-based and cobalt-based coatings were $4.570 \times 10^{-7} \text{ A cm}^{-2}$ and $8.911 \times 10^{-8} \text{ A cm}^{-2}$. The combination of Cr-rich passive film and fine dispersed carbides ensures high corrosion resistance of the cobalt-based coating.

Acknowledgments

The authors gratefully acknowledge to the financial support for this research from National Key Research and Development Program of China (No. 2016YFB1100204), Key Research Project from Science and Shenyang Science and Technology Funded Project (No.22-101-0-16, 19-109-1-03).

Author Contributions

FJ: Investigation, Writing—review & editing. SZ: Review & editing, Funding acquisition, Data curation. CLW: Review & editing, Funding acquisition, Data curation. CHZ: Funding acquisition, Data curation. XYS: Data curation. XLB: Data curation.

Conflict of interest

The authors declare that they have no known competing financial interests or personal relationships that could have appeared to influence the work reported in this paper.

References

1. A. Pardo, M.C. Merino, A.E. Coy, F. Viejo, R. Arrabal, and E. Matykina, Effect of Mo and Mn Additions on the Corrosion Behaviour of AISI 304 and 316 Stainless Steels in H_2SO_4 , *Corros. Sci.*, 2008, **50**(3), p 780–794

2. C. Hu, S. Xia, H. Li, T. Liu, B. Zhou, W. Chen, and N. Wang, Improving the Intergranular Corrosion Resistance of 304 Stainless Steel by Grain Boundary Network Control, *Corros. Sci.*, 2011, **53**(5), p 1880–1886
3. Y.A. Albrimi, A.A. Addi, J. Douch, R.M. Souto, and M. Hamdani, Inhibition of the Pitting Corrosion of 304 Stainless Steel in 0.5 M Hydrochloric Acid Solution by Heptamolybdate Ions, *Corros. Sci.*, 2015, **90**, p 522–528
4. M. Abdallah, Corrosion Behaviour of 304 Stainless Steel in Sulphuric Acid Solutions and its Inhibition by Some Substituted Pyrazolones, *Mater. Chem. Phys.*, 2003, **82**, p 786–792
5. Y. Liu, Y. Ding, L. Yang, R. Sun, T. Zhang, and X. Yang, Research and Progress of Laser Cladding on Engineering Alloys: A Review, *J. Manuf. Process.*, 2021, **66**, p 341–363
6. T. Zhao, S. Zhang, F.Q. Zhou, H.F. Zhang, C.H. Zhang, and J. Chen, Microstructure Evolution and Properties of in-situ TiC Reinforced Titanium Matrix Composites Coating by Plasma Transferred Arc Welding (PTAW), *Surf. Coat. Tech.*, 2021, **424**, p 127637
7. M. Li, B. Han, L. Song, and Q. He, Enhanced Surface Layers by Laser Cladding and Ion Sulfurization Processing towards Improved Wear-Resistance and Self-Lubrication Performances, *Appl. Surf. Sci.*, 2020, **503**, p 144226
8. C. Zhou, S.R. Wang, G.Q.J.P. Zhang, and W.L. Liu, Investigation on the Microstructure, Wear and Corrosion Resistance of FeCoNiCrMo_x High-Entropy Alloy Coatings Deposited on 40Cr by Laser Cladding, *J. Mater. Sci.*, 2022, **57**(39), p 18615–18639
9. T.Y. Yin, S. Zhang, F.Q. Zhou, R.J. Huo, C.H. Zhang, and J. Chen, Effects of Heat Treatment on Microstructure and Wear Behavior of Modified Aluminum Bronze Coatings Fabricated by Laser Cladding, *J. Mater. Eng. Perform.*, 2022, **31**, p 4294–4304
10. C. Wang, S. Zhang, C.H. Zhang, C.L. Wu, J.B. Zhang, and A.O. Abdullah, Phase Evolution and Wear Resistance of in situ Synthesized V_8C_7 Particles Reinforced Fe-Based Coating by Laser Cladding, *Opt. Laser Technol.*, 2018, **105**, p 58–65
11. L. Ding, S. Hu, X. Quan, and J. Shen, Effect of VN Alloy Addition on the Microstructure and Wear Resistance of Co-Based Alloy Coatings, *J. Alloy. Compd.*, 2016, **659**, p 8–14
12. L. Ding, S. Hu, X. Quan, and J. Shen, Effect of Aging Treatment on Microstructure and Properties of VN Alloy Reinforced Co-Based Composite Coatings by Laser Cladding, *Mater. Charact.*, 2017, **129**, p 80–87
13. H. Zhu, Y. Li, B. Li, Z. Zhang, and C. Qiu, Effects of Low-Temperature Tempering on Microstructure and Properties of the Laser-Cladded AISI 420 Martensitic Stainless Steel Coating, *Coatings*, 2018, **8**(12), p 451
14. H.F. Lu, K.N. Xue, X. Xu, K.Y. Luo, F. Xing, J.H. Yao, and J.Z. Lu, Effects of Laser Shock Peening on Microstructural Evolution and Wear Property of Laser Hybrid Remanufactured Ni25/Fe104 Coating on H13 Tool Steel, *J. Mater. Process. Tech.*, 2021, **291**, p 117016
15. W.R. Wang, W. Qi, X.L. Zhang, X. Yang, L. Xie, D.Y. Li, and Y.H. Xiang, Superior Corrosion Resistance-Dependent Laser Energy Density in $(\text{CoCrFeNi})_{0.5}\text{Nb}_5$ High Entropy Alloy Coating Fabricated by Laser Cladding, *Int. J. Min. Met. Mater.*, 2021, **28**(5), p 888–897
16. H. Wu, S. Zhang, Z. Wang, C.H. Zhang, H.T. Chen, and J. Chen, New Studies on Wear and Corrosion Behavior of Laser Cladding FeNiCoCrMo_x High Entropy Alloy Coating: The Role of Mo, *Int. J. Refract. Met. H.*, 2022, **102**, p 105721
17. X. Wang, C.H. Zhang, X. Cui, S. Zhang, J. Chen, and J.B. Zhang, Microstructure and Mechanical Behavior of Additive Manufactured Cr-Ni-V Low Alloy Steel in Different Heat Treatment, *Vacuum*, 2020, **175**, p 109216
18. X.D. Liang, S. Zhang, Z.Y. Wang, C.H. Zhang, D.X. Zhang, and C.L. Wu, Characterisation of Heat-Treated Gradient Alloy Steel Fabricated by Laser Melting Deposition, *Mater. Sci. Technol.*, 2023, **39**(5), p 567–581
19. H.F. Zhang, C.H. Zhang, Z.Y. Wang, X. Cui, S. Zhang, and H.T. Chen, Microstructure and Corrosion Behaviour of WC/NiCrBSi Coatings by Vacuum Cladding, *Mater. Sci. Tech.*, 2022, **38**(1), p 19–29
20. H. Song, J. Lei, J. Xie, S. Wu, L. Wang, and W. Shou, Laser Melting Deposition of K403 Superalloy: The Influence of Processing Parameters on the Microstructure and Wear Performance, *J. Alloy. Compd.*, 2019, **805**, p 551–564
21. A. Gholipour, M. Shamanian, and F. Ashrafzadeh, Microstructure and Wear Behavior of Stellite 6 Cladding on 17–4 PH Stainless Steel, *J. Alloy. Compd.*, 2011, **509**(14), p 4905–4909

22. X. Wang, M. Zhang, and S. Qu, Development and Characterization of (Ti, Mo) C Carbides Reinforced Fe-Based Surface Composite Coating Produced by Laser Cladding, *Opt. Laser Eng.*, 2010, **48**(9), p 893–898
23. X.Y. Yang, X. Peng, J. Chen, and F. Wang, Effect of a Small Increase in the Ni Content on the Properties of a Laser Surface Clad Fe-Based Alloy, *Appl. Surf. Sci.*, 2007, **253**(9), p 4420–4426
24. Q. Ma, Y. Li, J. Wang, and K. Liu, Investigation on Cored-Eutectic Structure in Ni60/WC Composite Coatings Fabricated by Wide-Band Laser Cladding, *J. Alloy. Compd.*, 2015, **645**, p 151–157
25. X. Cui, S. Zhang, C. Wang, C. Zhang, J. Chen, and J.B. Zhang, Effects of Stress-Relief Heat Treatment on the Microstructure and Fatigue Property of a Laser Additive Manufactured 12CrNi2 Low alloy Steel, *Mater. Sci. Eng. A*, 2020, **791**, p 139738
26. X. He, R.G. Song, and D.J. Kong, Microstructure and Corrosion Behaviour of Laser-Cladding Al-Ni-TiC-CeO₂ Composite Coatings on S355 Offshore Steel, *J. Alloy. Compd.*, 2019, **770**, p 771–783
27. J.Z. Lu, K.N. Xue, H.F. Lu, F. Xing, and K.Y. Luo, Laser Shock Wave-Induced Wear Property Improvement and Formation Mechanism of Laser Cladding Ni25 Coating on H13 Tool Steel, *J. Mater. Process. Tech.*, 2021, **296**, p 117202
28. P.F. Jiang, C.H. Zhang, S. Zhang, J.B. Zhang, J. Chen, and Y. Liu, Microstructure Evolution, Wear Behavior, and Corrosion Performance of Alloy Steel Gradient Material Fabricated by Direct Laser Deposition, *J. Mater. Res. Technol.*, 2020, **9**(5), p 11702–11716
29. X. Wang, C.H. Zhang, X. Cui, S. Zhang, J. Chen, and J.B. Zhang, Novel Gradient Alloy Steel with Quasi-Continuous Ratios Fabricated by SLM: Material Microstructure and Wear Mechanism, *Mater. Charact.*, 2021, **174**, p 111020
30. J.Z. Lu, J. Cao, H.F. Lu, L.Y. Zhang, and K.Y. Luo, Wear Properties and Microstructural Analyses of Fe-Based Coatings with Various WC Contents on H13 Die Steel by Laser Cladding, *Surf. Coat. Tech.*, 2019, **369**, p 228–237
31. Z. Wang, Z. Liu, C. Gao, K. Wong, S. Ye, and Z. Xiao, Modified Wear Behavior of Selective Laser Melted Ti6Al4V Alloy by Direct Current Assisted Ultrasonic Surface Rolling Process, *Surf. Coat. Tech.*, 2020, **381**, p 125122
32. G.F. Sun, Z.P. Tong, X.Y. Fang, X.J. Liu, Z.H. Ni, and W. Zhang, Effect of Scanning Speeds on Microstructure and Wear Behavior of Laser-Processed NiCr-Cr₃C₂-MoS₂-CeO₂ on 38CrMoAl Steel, *Opt. Laser Technol.*, 2016, **77**, p 80–90
33. Z. Tong, X. Pan, W. Zhou, Y. Yang, Y. Ye, D. Qian, and X. Ren, Achieving Excellent Wear and Corrosion Properties in Laser Additive Manufactured CrMnFeCoNi High-Entropy Alloy by Laser Shock Peening, *Surf. Coat. Tech.*, 2021, **422**, p 127504
34. Y. Zhou, S. Chen, X. Chen, T. Cui, J. Liang, and C. Liu, The Evolution of Bainite and Mechanical Properties of Direct Laser Deposition 12CrNi2 Alloy Steel at Different Laser Power, *Mater. Sci. Eng. A*, 2019, **742**, p 150–161
35. J. Archard, Contact and Rubbing of Flat Surfaces, *J. Appl. Phys.*, 1953, **24**(8), p 981–988
36. M. Ziętala, T. Durejko, M. Polański, I. Kunce, T. Płociński, W. Zieliński, M. Łazińska, W. Stępniewski, T. Czujko, and K.J. Kurzydłowski, The Microstructure, Mechanical Properties and Corrosion Resistance of 316 L Stainless Steel Fabricated using Laser Engineered Net Shaping, *Mater. Sci. Eng. A*, 2016, **677**, p 1–10
37. X. Wang, C.H. Zhang, F.Q. Zhou, S. Zhang, J. Chen, and J.B. Zhang, Novel Gradient Alloy Steel with Quasi-Continuous Ratios Fabricated by Selective Laser Melting: Microstructure and Corrosion Behavior, *Steel Res. Int.*, 2021, **92**(11), p 2100232
38. T. Ge, L. Chen, P. Gu, X. Ren, and X. Chen, Microstructure and Corrosion Resistance of TiC/Inconel 625 Composite Coatings by Extreme High Speed Laser Cladding, *Opt. Laser Technol.*, 2022, **150**, p 107919
39. M.H. Nie, S. Zhang, Z.Y. Wang, T.Y. Yin, C.H. Zhang, C.L. Wu, and D.X. Zhang, Laser Cladding of 17–4 PH Stainless Steel Coatings: Microstructure, Texture Characterization, and Corrosion Resistance, *J. Mater. Eng. Perform.*, 2023, **32**(12), p 5545–5553
40. C. Liao, J. Yang, Y. He, and X.Z. Ming, Electrochemical Corrosion Behavior of the Carburized Porous TiAl Alloy, *J. Alloy. Compd.*, 2015, **619**, p 221–227
41. M. Cao, L. Liu, Z. Yu, L. Fan, Y. Li, and F. Wang, Electrochemical Corrosion Behavior of 2A02 Al Alloy under an Accelerated Simulation Marine Atmospheric Environment, *J. Mater. Sci. Technol.*, 2019, **35**(4), p 651–659
42. X. Xu, H.F. Lu, K.Y. Luo, J.H. Yao, L.Z. Xu, J.Z. Lu, and Y.F. Lu, Mechanical Properties and Electrochemical Corrosion Resistance of Multilayer Laser Cladded Fe-Based Composite Coatings on 4Cr5Mo-SiV1 Steel, *J. Mater. Process. Tech.*, 2020, **284**, p 116736
43. Y. Gan, W. Wang, Z. Guan, and Z. Cui, Multi-Layer Laser Solid Forming of Zr65Al17.5Ni10Cu17.5 Amorphous Coating: Microstructure and Corrosion Resistance, *Opt. Laser Technol.*, 2015, **69**, p 17–22
44. X. Xu, H.F. Lu, Y.Y. Su, M.X. Peng, F. Xing, K.Y. Luo, and J.Z. Lu, Comparing Corrosion Behavior of Additively Manufactured Cr-rich Stainless Steel Coating between Conventional and Extreme High-Speed Laser Metal Deposition, *Corros. Sci.*, 2022, **195**, p 109976

Publisher's Note Springer Nature remains neutral with regard to jurisdictional claims in published maps and institutional affiliations.

Springer Nature or its licensor (e.g. a society or other partner) holds exclusive rights to this article under a publishing agreement with the author(s) or other rightsholder(s); author self-archiving of the accepted manuscript version of this article is solely governed by the terms of such publishing agreement and applicable law.